PAPER

Check for updates

Photoreforming of real biomass-derived waste streams using Nb-doped BiVO₄ photoanodes for sustainable hydrogen production

Lucas Leão Nascimento, [ID] [a] Rafael A. C. Souza, [ab] Paulo H. Horta Nunes, [a] João F. C. S. Costa, [d] Ivo A. Ricardo, [aef] Eduardo M. Oliveira, [ae] Klaus Krambrock, [ID] [d] Chuanyi Wang [ID] [c] and Antonio Otavio T. Patrocinio [ID] *[ae]

Solar-induced valorization of agroindustrial residues is a key issue for the so-called sustainable growth. In this study, a novel Nb-doped BiVO₄ photoanode is described and applied for the photoreforming of crude glycerol and flegmass, real byproducts of biodiesel production and sugarcane ethanol refining, respectively. To the best of our knowledge, this is one of the first reports exploring flegmass as a substrate for photoreforming. Nb(v) doping significantly enhances the photoanode performance, with 5% Nb : BiVO₄ exhibiting 80% increase in photocurrent during long-term crude glycerol photoreforming, reaching 2.2 mA cm⁻² at 1.0 V *vs.* RHE. When flegmass is employed, smaller photocurrents are observed in long-term experiments due to the lower organic content. Nevertheless, the 5% Nb : BiVO₄ photoanode exhibits a 200% increase in photocurrent compared to the pristine oxide. Detailed characterization reveals that Nb⁵⁺ doping occurs dominantly at VO₄ tetrahedral sites, also leading to oxygen vacancies as evidenced by EPR spectroscopy. Electrochemical impedance spectroscopy showed higher charge carrier densities and reduced charge transfer resistance in the Nb-modified photoanodes. Photoreforming of crude glycerol with 5% Nb : BiVO₄ after 6 hours of simulated sunlight irradiation achieved 91.4% substrate conversion, producing green H₂ at a rate of 4.2 μmol cm⁻² h⁻¹, much higher than 2.3 μmol cm⁻² h⁻¹ obtained by undoped BiVO₄. EPR spin trapping experiments indicated that the main reaction mechanism involves direct hole transfer to adsorbed glycerol on the catalyst surface, forming organic radical species. In flegmass photoreforming, 5% Nb : BiVO₄ achieved H₂ evolution rates of 2.4 μmol H₂ per cm² per h, consistently outperforming the bare BiVO₄ photoanode, highlighting its potential for valorizing low-cost, biomass-derived residues into valuable chemicals and renewable fuels.

Sustainability spotlight

The efficient and sustainable valorization of industrial waste streams is essential for promoting a circular economy and mitigating environmental impacts. This work reports a Nb-doped BiVO₄ photoanode for the solar-driven reforming of real industrial waste streams, crude glycerol and flegmass, into value-added compounds and green hydrogen. Niobium doping enhances charge carrier dynamics and photocatalytic activity, enabling a scalable strategy for waste treatment coupled with clean fuel production. This work directly supports the UN Sustainable Development Goals, particularly SDG 7 (Affordable and Clean Energy), SDG 9 (Industry, Innovation and Infrastructure), and SDG 12 (Responsible Consumption and Production).

[a] *Laboratory of Photochemistry and Materials Science, LAFOT-CM, LAFOT-CM Instituto de Química, Universidade Federal de Uberlândia, 38400-902, Uberlândia, MG, Brazil. E-mail: otaviopatrocinio@ufu.br*

[b] *Faculdade De Ciências Exatas e Tecnologia-FACET, Departamento de Ciências Exatas, Universidade Federal de Grande Dourados, 79084-970, Dourados, MS, Brazil*

[c] *School of Environmental Science and Engineering, Shaanxi University of Science and Technology, Xi'an, 710021, PR China*

[d] *Departamento de Física, Universidade Federal de Minas Gerais, 31270-901, Belo Horizonte, MG, Brazil*

[e] *Centro de Excelência em Hidrogênio e Tecnologias Energéticas Sustentáveis – CEHTES, Parque Tecnológico Samambaia, 74690-631, Goiânia, GO, Brazil*

[f] *Universidade Save, Faculdade de Ciências Naturais e Exatas, 0301-01 Chongoene, Gaza, Mozambique*

1 Introduction

There is an ever-growing demand to reduce waste production and improve the energy efficiency of industrial processes. The concept of a circular economy calls for implementing eco-friendly secondary processes that convert industrial residues and byproducts into valuable chemicals and green fuels, reducing emissions and supporting sustainable development.[1] The challenge lies in increasing the yield of these processes to enable practical applications downstream in industrial chains.

Photo-assisted reactions have been extensively studied for waste treatment and valorization.[1–7] In particular, the

photoreforming process utilizes industrial residues as sacrificial agents for low-carbon H_2 production, integrating principles of green chemistry with environmental remediation. Moreover, beyond H_2 generation, the selective oxidation of organic substrates can yield high-value chemicals, enhancing the overall economic viability of the process.

Photoelectroreforming is a promising approach that combines cost-effective and abundant photocatalysts with the enhanced kinetics offered by electrocatalysis. In this process, sunlight drives the desired reactions, while a small external bias improves charge separation and helps prevent undesired electron recombination.[5,8,9] This approach employs semiconductor oxides, such as TiO_2, WO_3, Fe_2O_3, and $BiVO_4$, immobilized on transparent conductive substrates to function as photoanodes in a photoelectrochemical cell. Among these, $BiVO_4$ stands out due to its favorable light absorption properties, relatively high photocurrent, and near-optimal theoretical solar-to-hydrogen (STH) efficiency.[10] However, $BiVO_4$ is highly susceptible to photocorrosion and exhibits short-lived carriers, resulting in sluggish kinetics and a lack of long-term stability.[11] Many approaches have been studied to address this phenomenon. Ke and co-workers reported that surface doping of $BiVO_4$ photoanodes with Mo^{5+} or W^{5+} significantly increased photocurrent and stability for water oxidation.[12] Liang and co-authors decorated the $BiVO_4$ surface with MoO_x nanoparticles, increasing the conversion of poly(ethylene-terephthalate) into formate, acetate, and H_2, which the authors attributed to improved charge transfer within the materials.[7] Kalanur and Seo reported Nb(v)-doped $BiVO_4$ photoanodes with enhanced water splitting performance when compared to pristine $BiVO_4$. Doping with Nb(v) increased the carrier density in the bulk of $BiVO_4$, improved the charge separation, charge transfer, and diffusion, and decreased the charge transfer resistance at the photoanode/electrolyte interface.[13] So far, such strategies have been poorly explored on photoelectroreforming, especially those employing real biomass-derived residues.

Biomass-derived industrial waste represents the largest renewable carbon source globally.[14] Most of these are lignocellulosic solid residues, known for their recalcitrant nature, which poses a considerable challenge to employing them as sacrificial agents in light-driven reactions.[1,15–17] However, several promising alternatives exist, particularly in the form of liquid waste streams. One notable example is glycerol, the primary byproduct of biodiesel production, currently available in large surplus. As an easily oxidizable triol in its refined form, glycerol has been widely recognized as an effective electron donor for photoreforming.[4,5,18,19] Additionally, some oxidation products of glycerol, such as dihydroxyacetone (DHA), glyceraldehyde, and formic acid, are valuable chemicals with diverse applications. Glycerol global production reached approximately 3 to 4 million tons annually as of recent estimates.[20,21] Costly refinement processes, however, are often required to convert crude glycerol for commercial uses, involving purification steps such as distillation and ion exchange. Moreover, photoreforming of crude glycerol is difficult to accomplish, as pointed out by Ribao and co-workers, due to the presence of impurities and the increased turbidity of crude glycerol suspensions that

severely compromise conversion efficiency.[22] Furthermore, the high viscosity of glycerol hinders its diffusion through the photocatalyst, requiring significant dilution to achieve practical conversion rates. Thus, there is a need for processes that enable the direct conversion of crude glycerol, eliminating costly additional steps.

Flegmass is another example of a widely available liquid waste stream. This aqueous distillation residue originates from the sugarcane processing industry (bio-ethanol production) and is composed of residual short-chain alcohols (*e.g.*, methanol and ethanol), traces of organic acids, esters, aldehydes, and ketones, as well as isoamyl alcohol and its derivatives.[23] Not to be mistaken for distillery stillage, flegmass is one of the most significant waste streams in the sugarcane processing plants, especially in Brazil, where its production reaches around 150 million cubic meters annually.[24] The use of flegmass as a sacrificial agent for photoreforming is advantageous because this aqueous residue can be used directly, eliminating the need for prior processing and/or dilution. However, to our knowledge, there are no studies exploring the valorisation of flegmass.[23,25]

Herein, for the first time, a photoelectrochemical cell assembled with Nb(v)-doped $BiVO_4$ ($Nb:BiVO_4$) was applied for the photoreforming of crude glycerol and flegmass residues, collected from a biodiesel plant and a sugarcane processing refinery, respectively. The morphological and electronic properties of the photoanode were evaluated as a function of dopant concentration, followed by photoelectrochemical assays employing real residues for hydrogen production and biomass valorization.

2 Results and discussion

The $BiVO_4$ samples with different Nb^{5+} contents were analysed through XRD and Raman spectroscopy to elucidate their structural properties. The diffractograms of all samples (Fig. 1a) were mainly indexed to the monoclinic phase with some tetragonal contribution, especially for pure $BiVO_4$. The preferred orientation for all samples was the (1 1 2) plane at 28.97° with major contributions from the (0 0 4) crystalline plane at 34.55°, consistent with monoclinic $BiVO_4$.[26–28] Moreover, the diffraction peaks shift to slightly lower angles as the Nb^{5+} content increases, indicating an expansion of the lattice parameters due to lattice distortion caused by Nb^{5+} insertion. This effect is attributed to the larger radius of Nb^{5+} (0.69 Å)[29] when compared to V^{5+} (0.50 Å), similarly to what is observed for W^{6+} doping of $BiVO_4$ (ref. 30), and in agreement with previous DFT studies carried out by Kalanur and Seo,[13] indicating that Nb^{5+} incorporates into the $BiVO_4$ lattice by replacing V^{5+} sites.

Raman spectra (Fig. 1b) show peaks characteristic of the monoclinic phase, particularly the signal at 830 cm^{-1} assigned to the asymmetric stretching of the tetrahedral V–O bonds. Bands around 320 and 367 cm^{-1} were attributed to asymmetric and symmetric deformation modes of the VO_4^{3-} tetrahedron. Additionally, the $BiVO_4$ sample also shows a less intense stretching peak at 248 cm^{-1} relative to the Bi–O symmetric vibration of the tetragonal phase. These bands are broadened as Nb content increases, with a pronounced effect on the bands
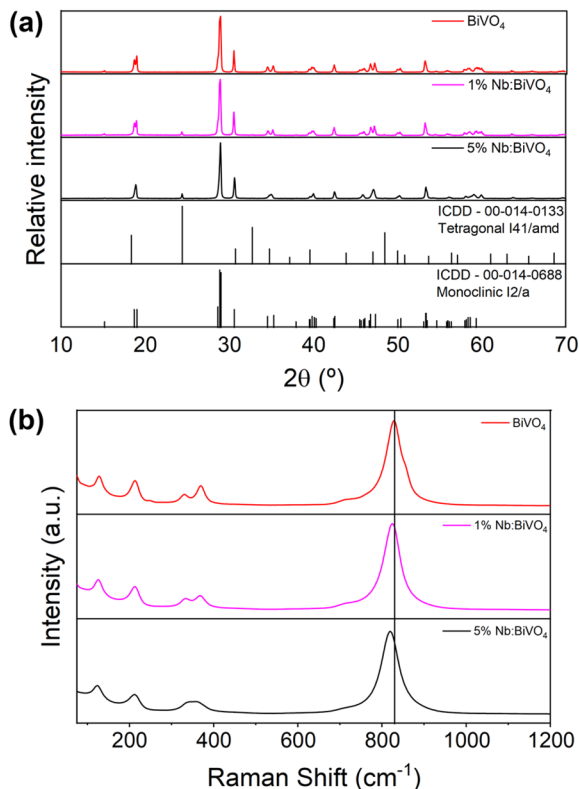
Fig. 1 (a) XRD patterns and (b) Raman spectra of pristine $BiVO_4$ and Nb : $BiVO_4$ samples.
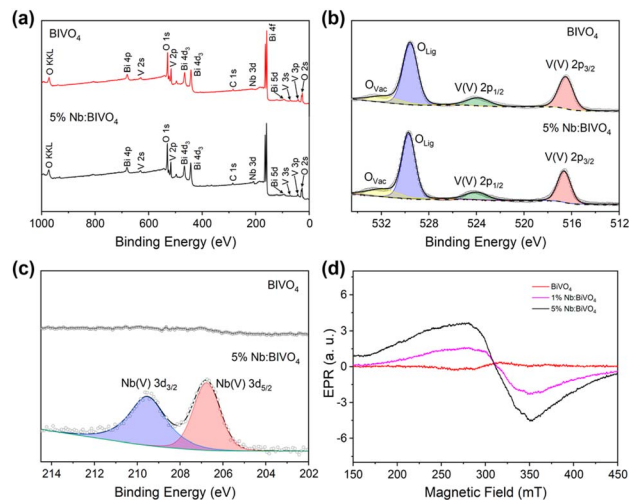

Fig. 2 (a) Survey spectra of $BiVO_4$ and 5% Nb : $BiVO_4$; (b) high-resolution XPS spectra of V 2p and O 1s; (c) high-resolution XPS spectra of Nb 3d; and (d) EPR spectra of the solid-state powder $BiVO_4$-based catalysts.

associated with the deformations in the VO_4^{3-} tetrahedra. This change indicates loss of the short-range arrangement due to Nb^{5+} doping at V^{5+} sites. Additionally, the slight shift of Raman features toward lower wavenumbers suggests changes in the short-range symmetry of the VO_4^{3-} tetrahedra,[26,31] further supporting the hypothesis that Nb^{5+} doping occurs at V^{5+} sites. Additional characterization studies were carried out for the 5% Nb : $BiVO_4$ sample and compared with pristine $BiVO_4$.

X-ray photoelectron spectroscopy (XPS) was performed to analyze the surface composition and electronic properties of the different $BiVO_4$ samples. Fig. 2a shows the XPS survey spectra of all synthesized materials, indicating no significant contamination. The high-resolution XPS spectra in Fig. 2b show two distinct oxygen peaks for both the pristine and the 5% Nb-doped $BiVO_4$ samples. The peak at lower binding energy corresponds to lattice oxygen (O_{lig}), while the less intense peak at higher binding energy is attributed to oxygen-adsorbed species and can be correlated with oxygen vacancies (O_{vac}) in the $BiVO_4$ surface.[32,33] The relative intensity of the oxygen vacancy peak is twice as high in the 5% Nb : $BiVO_4$ sample compared to $BiVO_4$, suggesting an increased concentration of oxygen vacancies due to niobium doping. In the spectral region of the Nb 3d peak (Fig. 2c) the expected doublet for Nb^{5+} species is observed, further confirming the presence of Nb(v) at the surface of 5% Nb : $BiVO_4$.[13,34,35] Elementary quantification of the surface reveals a niobium content of 5.1 ± 0.1% wt% for the 5% Nb : $BiVO_4$ sample, while the vanadium content decreased by

4.9 ± 0.1% relative to the pristine sample (Table S1) corroborating the hypothesis that Nb^{5+} replaces V^{5+} in the lattice.

EPR spectra measured at room temperature with a microwave frequency of about 9.43 GHz for the different solid-state powders are shown in Fig. 2d. The spectra show a broad paramagnetic resonance line (line with about 75(5) mT) with a g factor of about 2.05(5), typical of paramagnetic salts of transition metal ions (Nb^{4+} and V^{4+}) or paramagnetic niobium–oxygen vacancy complexes. The highest EPR signal intensity is observed for the $BiVO_4$ sample doped with 5% of niobium, followed by the sample with 1% of Nb doping. The pristine sample does not show this broad paramagnetic signal. The results suggest that part of the Nb doped into the $BiVO_4$ samples is incorporated in the samples as Nb^{4+}, which is paramagnetic with spin $S = \frac{1}{2}$ compared with Nb^{5+} that is diamagnetic. At first glance, this result is contradictory to the XPS analysis, in which only Nb^{5+} signals were clearly observed, but this is actually explained by the sensitivity of each technique. By comparing the EPR signal intensity with that of an anhydrous $CuSO_4$ standard powder sample, the concentration of the broad EPR signal in the 5% Nb : $BiVO_4$ sample is estimated to be approximately 10^{15} cm^{-3}. Assuming that Nb^{4+} is principally incorporated at the surface, possibly complexed with oxygen vacancies, the concentration of these defects in the surface region would be about 3 orders of magnitude higher. This concentration is still below the detection limit for XPS spectroscopy, explaining the missing Nb^{4+} transitions in the XPS spectra. One can conclude, then, that the increased oxygen vacancy concentration on the Nb : $BiVO_4$ samples can be associated with the formation of Nb^{4+} species. High-Resolution Transmission Electron Microscopy (HRTEM) images (Fig. 3a–d) show both $BiVO_4$ and 5% Nb : $BiVO_4$ samples with interplanar spaces of 0.31 nm attributed to the (112) plane of monoclinic $BiVO_4$, in good agreement with the XRD spectra in which high relative intensities for the (112) lattice plane are observed for all samples.[36,37] Moreover, EDS elemental mapping
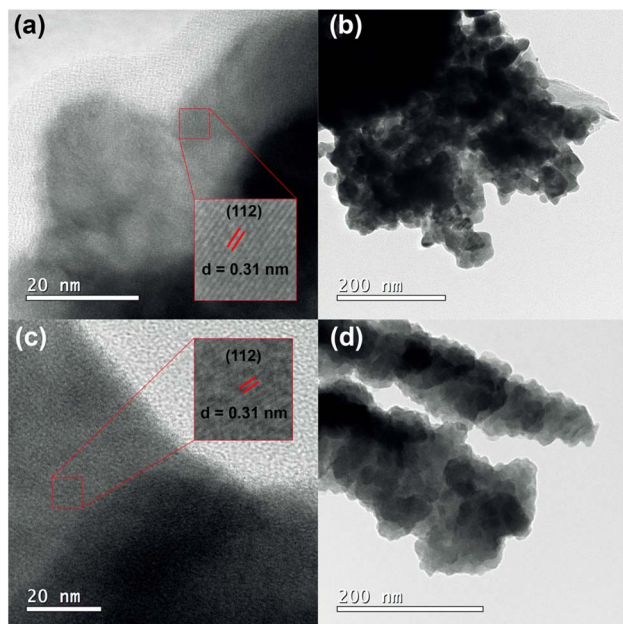
Fig. 3 HRTEM images of (a and b) $BiVO_4$ and (c and d) 5% $Nb : BiVO_4$ at different magnification levels.

of 5% $Nb : BiVO_4$ powder (Fig. S1(a and f)) shows the presence of niobium at the surface of the material.

The powder samples were then deposited onto clean FTO substrates using the screen-printing method. Scanning Electron Microscopy (SEM) images of the screen-printed photoanodes (Fig. S2a and f) show that the $BiVO_4$-based films are formed by the agglomeration of spherical particles formed during the sintering step. Cross-section SEM images (Fig. S3) were taken to measure the thickness of the films. The measured average thickness was 1.9 ± 0.2 μm. EDS mapping of the film surface and the cross-section evidenced the homogeneous distribution of Nb, Bi and V on the film, as expected. Diffuse reflectance measurements (Fig. 4a) indicate that Nb^{5+} doping did not induce any drastic changes in the optical properties of $BiVO_4$. The strong absorption band up to 500 nm accounts for the intense yellow color of the photoanodes, Fig. 4a (inset). All synthesized samples displayed a band gap energy (E_g) of 2.45 ± 0.05 eV (Fig. 4b) consistent with other $BiVO_4$ samples obtained through hydrothermal synthesis.[27,28,38]
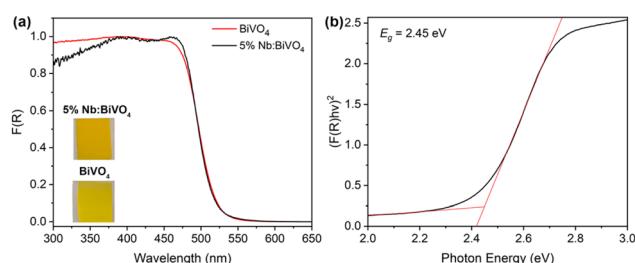
Electrochemical Impedance Spectroscopy (EIS) was employed to gain insights into the charge transport process in the obtained photoanodes. The EIS data (Fig. S4) show that both pristine $BiVO_4$ and Nb-doped samples exhibit similar behavior under dark conditions, as expected, since the crystalline properties were not significantly affected by Nb^{5+} doping. However, under illuminated conditions (Fig. 5a) the 5% $Nb : BiVO_4$ sample demonstrated significantly lower total impedance, when compared to the 1% $Nb : BiVO_4$ and undoped samples, with both displaying a more capacitive response, characterized by higher phase angles when compared to the 5% $Nb : BiVO_4$ sample (Fig. 5b).

The EIS data were fitted using a simplified Randle's circuit as a model (Fig. 5a, inset), in which R_s is the resistance of the electrolyte, C_{dl} is the capacitance of the double-layer, and R_{ct} is the charge transfer resistance. The fitting data parameters (Table S2) indicate no relevant changes in the electrochemical properties between $BiVO_4$ and 1% $Nb : BiVO_4$. However, the 5% $Nb : BiVO_4$ films showed a much lower charge transfer resistance of 634 Ω under simulated sunlight, when compared to 1290 Ω obtained by the pristine $BiVO_4$ film under the same conditions. This behavior was further investigated using Mott–Schottky plots (Fig. 5c and d) which show that the 5% $Nb : BiVO_4$ films exhibit a charge carrier density of -8.15×10^{19} cm^{-3}, twofold higher than that compared to the pristine sample of -4.40×10^{19} cm^{-3}. In contrast, the flat-band potential (V_{fb}) was not significantly affected by Nb^{5+} doping, with both samples displaying similar V_{fb} values ranging from -0.012 ($BiVO_4$) to 0.069 V $vs.$ RHE (5% $Nb : BiVO_4$), consistent with the literature.[13,39,40] Thus, Nb^{5+} doping greatly improved charge transport, resulting in an increased charge carrier density across the photoanode surface, but without significantly shifting either the conduction band or the bandgap energy of $BiVO_4$.
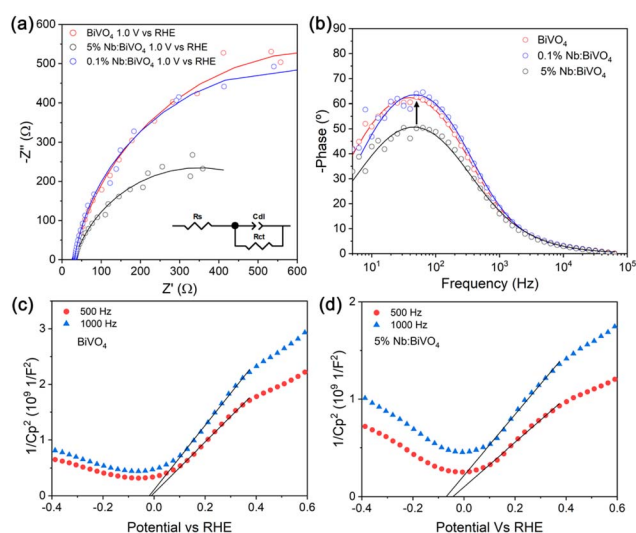

Fig. 5 (a) EIS Nyquist plots of $BiVO_4$, 1% $Nb : BiVO_4$ and 5% $Nb : BiVO_4$ in 0.1 M K_2SO_4 at different potentials and illumination (AM 1.5 G 100 mW cm^{-2}). (b) Bode plots under the same conditions. Mott–Schottky plots of (c) $BiVO_4$ and (d) 5% $Nb : BiVO_4$ under illumination.

Fig. 4 (a) Diffuse reflectance spectra of $BiVO_4$ and 5% $Nb : BiVO_4$ films and (b) Tauc plot of $BiVO_4$.

EPR spin trapping experiments with DMPO (0.1 M) in distilled water suspensions (pH $\sim$ 6), containing 5% Nb : BiVO$_4$ powder under magnetic stirring, show the formation of radical adducts under white light illumination. Fig. 6a and b display the EPR spectra of DMPO spin adducts as a function of time in pure water and mixed water/glycerol (10%) suspensions. The radical adducts were identified by spectral simulation of the spectra using the Easyspin® routine in Matlab (Fig. 6c). The two DMPO adducts were identified as DMPO–$^\bullet$OH and DMPO–$^\bullet$R. The EPR spectrum of the DMPO–$^\bullet$OH adduct is characterized by a hyperfine interaction between the electron spin $S = \frac{1}{2}$ and the nuclear spin $I = 1$ (from ^{14}N) and the nuclear spin $I = \frac{1}{2}$ (from ^{1}H) leading to $a_N = a_{H\beta} = 1.49$ mT, resulting in the well-known four-line spectrum with intensity ratios of $1 : 2 : 2 : 1$.[41] The EPR spectrum of the DMPO–$^\bullet$R adduct is described by a six-line spectrum with equal intensities and hyperfine parameters of $a_N = 1.57$ mT and $a_{H\beta} = 2.29$ mT. This latter DMPO adduct is less specific, but it is probably of organic nature, attributed to a carbon-centered radical adduct of DMPO ($a_{H\beta} > a_N$)[42] and references therein, different from the DMPO–$^\bullet$OH adduct, which is oxygen-centered ($a_N > a_{H\beta}$). In a mixed water/glycerol (10%) suspension, DMPO formed two different spin adducts, while only one spin adduct was observed in pure water. These results indicate that the organic radical is produced from glycerol, while hydroxyl radicals are produced from water. The concentration of the organic radicals depends on the ratio of the water/glycerol mixture. A higher glycerol ratio increased the related EPR DMPO–$^\bullet$R adduct concentration (not shown).

Acidic pH also favors the formation of these organic radicals. The reaction kinetics are strongly influenced by the pH of the solution. When the same spin trapping experiments were performed at pH $\sim$2, the same DMPO spin adducts were observed as at pH $\sim$6; however, with increased concentrations (Fig. 6d), a similar result was reported elsewhere.[13] In contrast, in mixed water/glycerol (10%) suspensions at pH $\sim$2, we also noticed some formation of spin adducts in the dark (not shown).

When the spin trapping experiments were carried out with the 5% Nb : BiVO$_4$ photoanode coupled with a Pt cathode under a bias of about $\sim$1.0 V vs. RHE in the presence of DMPO (0.2 M) in mixed water/glycerol (10%) solution and K$_2$SO$_4$ electrolyte (0.1 M) at pH $\sim$6, the EPR results (Fig. 6e) reveal the formation of the same spin adducts observed before, but with higher intensities, indicating an accelerated kinetics of the reactions and higher yield for the formation of $^\bullet$OH radicals. Comparing different BiVO$_4$ photoanodes (Fig. 6f) the higher Nb^{5+} doped sample (5%) showed higher efficiency ($\sim$35%) in the formation of DMPO–$^\bullet$OH adducts under white light illumination than the undoped BiVO$_4$ or 1% Nb : BiVO$_4$ ones. These results indicate a significantly enhanced ability to generate organic radicals and hydroxyl radicals, which aligns with the EIS results, as the 5% Nb : BiVO$_4$ photoanode also exhibited a higher charge carrier density compared to pristine BiVO$_4$. Moreover, radical formation is largely dependent on the applied bias and illumination, correlating with the much lower charge transfer resistance due to surface defects (oxygen vacancies and/or Nb^{4+} ions) as observed for 5% Nb : BiVO$_4$ films under illumination.

Our findings with DMPO EPR spin trapping align well with the reaction mechanism proposed before (ref. 13). Dong Liu et al. utilized a nanoporous BiVO$_4$ photoanode for the photoelectrochemical oxidation of glycerol and discovered that glycerol strongly adsorbs onto the BiVO$_4$ surface. In the initial step of the reaction, the adsorbed glycerol molecules are converted into glycerol radicals through direct hole oxidation. These radicals then react with water from the electrolyte, followed by a dehydration step, leading to different subproducts of glycerol. In our experiments using DMPO EPR spin trapping, we also observed the generation of organic radicals, although their exact nature remains unknown. Additionally, we detected hydroxyl radicals (see Fig. 6a and b), which may play an important role in guiding the complex photoreforming reaction mechanisms of glycerol towards different subproducts.

Fig. 6 Formation of DMPO spin adducts during spin trapping experiments for 5% Nb : BiVO$_4$ photocatalyst powder under white light (0–20 min) for (a) distilled H$_2$O and (b) H$_2$O containing 10% of glycerin at pH $\sim$6; (c) EPR spectra calculations using Easyspin® identifying DMPO–$^\bullet$OH and DMPO–$^\bullet$R spin adducts; (d) same as in (b) but at pH $\sim$2; (e) same as in (b) but using a 5% Nb : BiVO$_4$ photoanode coupled with a Pt cathode with an applied bias of about 1.0 V vs. RHE; and (f) DMPO–$^\bullet$OH spin adduct concentration as a function of time using different Nb-doped BiVO$_4$ photoanodes.

2.1. Photoelectroreforming experiments

The pristine and Nb-doped BiVO$_4$ films were applied as photoanodes in photoelectrochemical cells for photoelectroreforming of crude glycerol and flegmass (Fig. S5). For reference, experiments with purified glycerol (glycerin) were also carried out. The glycerol residue was collected at a soybean
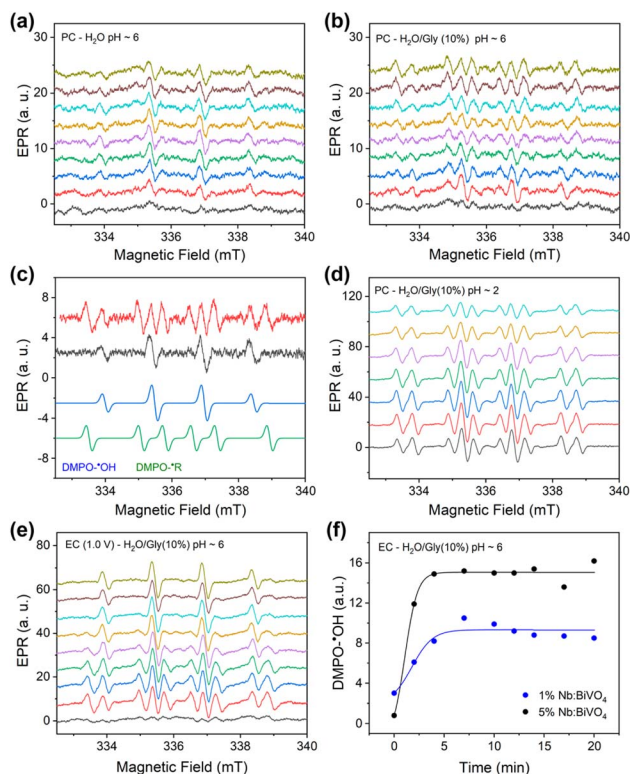
biodiesel plant, and its composition consists of glycerin, with several contaminants such as water, ethanol, methanol and many solid impurities. Flegmass residue is an aqueous byproduct from sugarcane ethanol distillation, consisting of a mixture of various organic compounds, which include ethanol, organic acids and fusel alcohols, such as isobutanol, isoamyl alcohol, and propanol. Although the organic content of the employed sample was relatively high (chemical oxygen demand of 3000 mg mL^{-1}), the concentration of each organic species is small. Ethanol was identified as the main constituent of flegmass, albeit in concentrations below 5% m m^{-1}, along with traces of isoamyl alcohol. Flegmass composition is highly dependent on the species of sugarcane used, the fermentation conditions and the following processing steps.

Light-chopped linear sweep voltammograms (LSVs) (Fig. 7) show all tested photoanodes with a similar photoresponse profile, consisting of a sharp increase in photocurrent upon light exposure and a prompt decrease when the light is switched off. The LSVs with glycerin (Fig. 7a) show that the 5% Nb : BiVO$_4$ photoanode achieved the highest photocurrent, approximately 70% higher than that of the pristine BiVO$_4$ sample, which in turn produced similar photocurrents to the 1% Nb : BiVO$_4$ photoanodes. When crude glycerol was used (Fig. 7b), the same trend was observed, although the overall photocurrent was 20% lower. Finally, with flegmass (Fig. 7c), the 5% Nb : BiVO$_4$ photoanodes yielded the same level of photocurrent as with pure glycerin, showing nearly 100% increase compared to the other photoanodes. Under all tested conditions, the 5% Nb : BiVO$_4$ films consistently outperformed the others, while the 1% Nb : BiVO$_4$ and pristine BiVO$_4$ films produced similar results, suggesting that lower Nb^{5+} doping levels did not significantly impact BiVO$_4$ performance.

Long-term photoreforming of crude glycerol was conducted using pristine BiVO$_4$ and 5% Nb : BiVO$_4$ films, as the latter exhibits the best-performance among the Nb-doped photoanodes. The 5% Nb : BiVO$_4$ sample yielded a higher oxidative photocurrent (Fig. 8a) converting 91.4% of glycerol, compared to 73.3% for pristine BiVO$_4$, after 6 hours of irradiation (A.M. 1.5 100 mW cm^{-2}). The H$_2$ evolution rate was also significantly higher for 5% Nb : BiVO$_4$, reaching 4.2 μmol H$_2$ per cm^2 per h versus 2.3 μmol H$_2$ per cm^2 per h with BiVO$_4$ (Fig. 8b). The faradaic efficiency for H$_2$ evolution was 96% for 5% Nb : BiVO$_4$
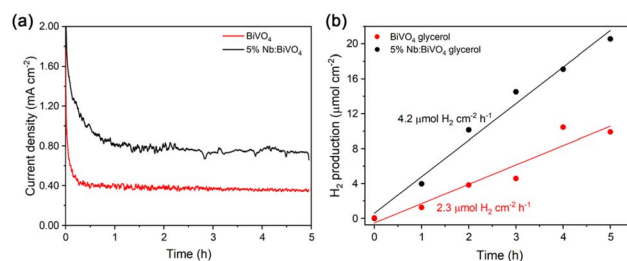

Fig. 8 (a) Chronoamperometry graphs of BiVO$_4$ and 5% Nb : BiVO$_4$ in crude glycerol 10%/v in K$_2$SO$_4$ 0.1 M under 1.0 V vs. RHE and 100 mW cm^2 AM 1.5 G illumination. (b) H$_2$ evolution from an average of 3 chronoamperometry experiments for BiVO$_4$ and 5% Nb : BiVO$_4$ photoanodes.

and 98% for BiVO$_4$, indicating that crude glycerol photoreforming is viable for sustained green H$_2$ production.

Regarding oxidation products, formic acid was the main product for both pure glycerin and raw glycerol, with a C-based selectivity of 89% for 5% Nb : BiVO$_4$ and 71% for BiVO$_4$. Other minor products, including oxalic acid (2%), acetic acid (5%), and dihydroxyacetone (<1%), were also detected, as shown in NMR and HPLC data in the supplementary information (Fig. S6 and S7). Moreover, CO$_2$ evolution was also qualitatively detected during the photoelectroreforming assays, suggesting that the remaining amount of the consumed glycerol was eventually mineralized. XPS analysis of the films subjected to 8-hour-long crude glycerol photoelectroreforming assays was conducted to evaluate the long-term stability of the photoanode. The results were compared to fresh prepared photoanodes (Fig. S8). The films exposed to the glycerol solution exhibited a higher relative carbon content as part of the organic species remained adsorbed on the surface. It was possible, however, to clearly identify the presence of Nb^{5+}, Bi^{3+} and V^{5+} signals, with similar chemical shifts as those observed in the fresh photoanode. The determined Nb : Bi ratio in the surface of the photoanode after the photoelectrochemical assay was 0.15, while for the fresh sample, it was 0.17. SEM images and EDS analysis of the used photoanode (Fig. S2d–f) showed that the film morphology and composition remained very similar to those observed for fresh prepared samples. Moreover, ICP-OES analysis of the anolyte has only detected traces (<0.5 ppm) of Bi(III) and Nb(V),
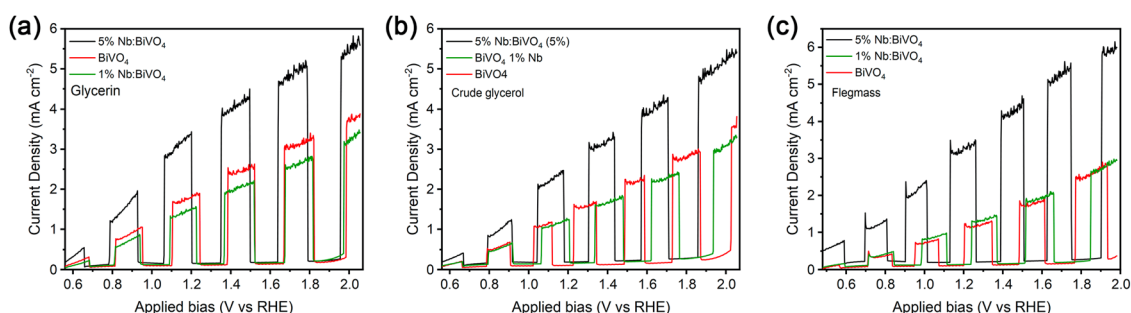

Fig. 7 Light-chopped linear sweep voltammograms of pristine BiVO$_4$, 1% and 5% Nb : BiVO$_4$ films in (a) glycerin 10% v/v in K$_2$SO$_4$ 0.1 M, (b) crude glycerol 10% v/v in K$_2$SO$_4$ 0.1 M and (c) raw flegmass with added 0.1 M K$_2$SO$_4$.
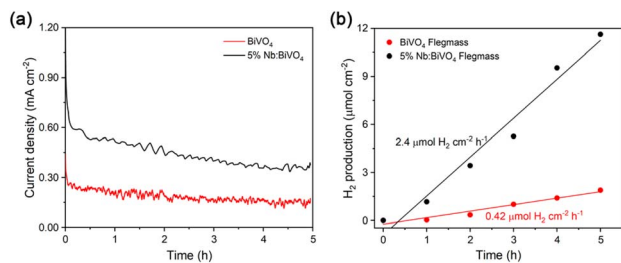
Fig. 9 (a) Chronoamperometry graphs of BiVO$_4$ and 5% Nb : BiVO$_4$ in raw flegmass, under 1.0 V vs. RHE and 100 mW cm^2 AM 1.5 G illumination. (b) H$_2$ evolution from an average of 3 chronoamperometry experiments for BiVO$_4$ and 5% Nb : BiVO$_4$ photoanodes.
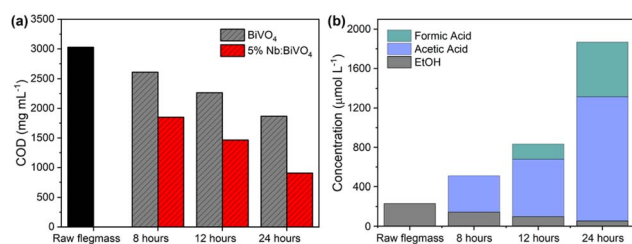

Fig. 10 (a) COD removal from flegmass after photoelectroreforming experiments with different durations using the BiVO$_4$ and 5% Nb : BiVO$_4$ photoanodes. (b) HPLC results showing the variation in concentration of flegmass main oxidation products as a function of time during photoelectroreforming experiments using 5% Nb : BiVO$_4$ photoanodes under simulated sunlight (AM 1.5 G 100 mW cm^{-2}) and 1.0 V vs. RHE applied bias.

evidencing the stability of the 5% Nb : BiVO$_4$ in the K$_2$SO$_4$ electrolyte containing 10% v/v crude glycerol.

When flegmass was used as a sacrificial agent in long-term photoreforming experiments, the current density was consistently higher for 5% Nb : BiVO$_4$ (Fig. 9a), which also resulted in a higher H$_2$ evolution rate of 2.4 μmol H$_2$ per cm^2 per h, compared to 0.42 μmol H$_2$ per cm^2 per h achieved with the pristine BiVO$_4$ photoanode (Fig. 9b). As flegmass is a more diluted and complex matrix than glycerol, the quantification and identification of liquid oxidation products proved challenging. HPLC analysis of the crude residue revealed the

presence of ethanol and isoamyl alcohol as the main components (Fig. S9). Alternatively, the consumption of organic species during photoelectroreforming was evaluated based on Chemical Oxygen Demand (COD) removal. 5% Nb : BiVO$_4$ exhibited superior COD removal of up to 70%, compared to 38% for BiVO$_4$ after 24 h irradiation (Fig. 10a). HPLC analysis in different time intervals (Fig. 10b) reveals the build-up of acetic acid as the primary oxidation product, with some formic acid appearing at longer irradiation times. These results are promising, especially given that flegmass was used as received, without dilution or pre-treatment, an important consideration for enabling practical applications. The superior performance observed for the 5% Nb : BiVO$_4$ photoanodes can be explained by the increased charge carrier density, decreased charge transfer resistance at the BiVO$_4$/electrolyte interface, and the higher presence of reactive surface states due to Nb^{5+} doping.

Other researchers have explored similar strategies to enhance the biomass photoelectroreforming capabilities of BiVO$_4$. Some representative results are shown in Table 1. Bora and co-workers reported Mo-doped BiVO$_4$ photoanodes with improved current density in the presence of glycerol.[18] This enhancement was attributed to the formation of a capacitance layer and a reduction in charge transfer resistance on the photoelectrode, described as a photocharging phenomenon. However, no direct comparison was made with pristine BiVO$_4$ photoanodes. Similarly, Tateno et al. investigated the effect of Ta-doping on BiVO$_4$ photoanodes for the photoelectrochemical oxidation of glycerol.[43] They observed a significant increase in photocurrent of over 60% compared to undoped BiVO$_4$, along with enhanced photoanode stability in acidic electrolytes. Notably, Ta doping did not significantly alter the band positions or structural properties of BiVO$_4$, similarly to what we have observed for Nb-doped samples. However, Nb doping resulted in a superior increase of 80% in photocurrent, evidencing its effectiveness in improving BiVO$_4$-based photoanodes.

In summary, Nb doping at 1% and below did not significantly affect the properties of BiVO$_4$. However, when the Nb content was increased to 5 wt%, charge transfer across the photoanode bulk and surface was enhanced, as evidenced by the higher charge carrier density and significantly lower charge transfer resistance of the 5% Nb : BiVO$_4$ photoanode compared

Table 1 Photocurrent density of metal–doped BiVO$_4$ photoanodes compared to this work, under glycerol photoreforming conditions with AM 1.5 G, 100 mW cm^{-2} illumination and 1.0 V vs. RHE

Photoanode	Undoped BiVO$_4$ photocurrent density^a	Metal-doped BiVO$_4$ photocurrent density^a	Experimental remarks^b	Ref.
W : BiVO$_4$	NA	3.1 mA cm^{-2}	0.5 M potassium borate buffer with 0.1 M glycerol	46
Mo : BiVO$_4$	NA	4.6 mA cm^{-2}	Glycerol 20% v/v with 0.1 M phosphate buffer. After photocharging effect	18
Ta : BiVO$_4$	1.6 mA cm^{-2}	2.6 mA cm^{-2}	Glycerol 1.0 M with H$_2$SO$_4$ 25 mM	43
Nb : BiVO$_4$	1.2 mA cm^{-2}	2.2 mA cm^{-2}	Glycerol 10% v/v with 0.1 M K$_2$SO$_4$	This work
Nb : BiVO$_4$	0.8 mA cm^{-2}	2.4 mA cm^{-2}	Flegmass with added 0.1 M K$_2$SO$_4$	This work

^{a} Estimated based on reported LSV curves (± 0.1 mA cm^{-2}). ^{b} The performance values were taken directly from the respective references and were obtained under varying experimental conditions (e.g., electrolyte composition, sacrificial agent, light source, and measurement protocols). Direct quantitative comparison between different studies should therefore be made with caution.

to pristine BiVO$_4$, which was attributed to the introduction of Nb^{5+} in the lattice and surface defects (oxygen vacancies and/or Nb^{4+} species). This improvement was reflected in the photoreforming results, where 5% Nb : BiVO$_4$ demonstrated more than twice the photocurrent and hydrogen evolution.

The improved photoelectrochemical performance 5% Nb : BiVO$_4$ photoanodes compared to pristine BiVO$_4$ was also observed when real waste streams (crude glycerol and flegmass) were employed in the photoelectrochemical cells. The use of real biomass residues in photoelectroreforming is an unexplored field in the literature. A few examples can be found using photocatalytic systems based on suspensions of semiconductor nanoparticles. Skaf *et al.* showed that for photocatalytic reforming, activity losses of up to 3.5 times occur when crude glycerol is used instead of purified glycerol.[44] Villachica-Llamosas *et al.* evaluated the hydrogen evolution from pure glycerol solutions prepared with natural waters, revealing decreased efficiencies when compared to high-purity water.[45] Our system stands out by demonstrating high selectivity and performance with non-treated crude glycerol, with no additional conditioning, indicating that Nb-doped BiVO$_4$ tolerates real waste conditions. The excellent performance is accompanied by improved stability under irradiation, which serves as proof of concept for the possible large-scale application of photoelectroreforming.

3 Experimental

All chemicals were used as received and bought from Aldrich in analytical or HPLC grade. Nanocrystalline BiVO$_4$ and Nb : BiVO$_4$ were prepared by adding 5 mmol of Bi(NO$_3$)$_3$ in 10 mL of 4 M HNO$_3$ solution, 5 mmol of NH$_4$VO$_3$ in 10 mL of 2 M NaOH and 2 mL of H$_2$O$_2$ 30%. After complete dissolution of the precursors, the V^{5+} solution was added to the Bi^{3+} solution dropwise, under vigorous stirring. The resulting mixture was neutralized using a 2 M NaOH solution. Following, the mixture was transferred to a PTFE vessel, which was then placed in a sealed hydrothermal reactor and subjected to hydrothermal treatment at 200 °C (180 psi) for 4 h. The Nb : BiVO$_4$ samples were obtained by adding niobium(v) ammonium oxalate to the precursor solution, yielding 1 and 5% w/w Nb content in the resulting materials. The obtained powders were washed with deionized water and ethanol, and dried at 80 °C.

The BiVO$_4$-based photoanodes were deposited on clean FTO substrates using the screen printing method.[47] The paste for screen printing was prepared following the methodology previously described elsewhere.[48] Briefly, 3 g of photocatalyst powder were thoroughly ground in a mortar containing 15 mL of ethanol, 2.5 mL of water and 0.5 mL of acetic acid, and then transferred to a round flask with the further addition of 50 mL of ethanol, 10 g of terpineol and 15 g of a 10 wt% ethyl cellulose solution in ethanol. The mixture was sonicated and stirred until the material was completely dispersed. Finally, the solvent was removed with a rotary evaporator. The films were manually deposited using a 200 mesh per inch polyester screen, followed by annealing at 500 °C for 30 min to remove organic components and increase their mechanical stability.

X-ray diffraction analysis (XRD) was performed with an XRD600 powder diffractometer (Shimadzu) operating at 40 kV and 30 mA employing Cu Kα radiation. Raman spectroscopy was conducted using a LabRAM HR Evolution spectrometer (Horiba). X-ray photoelectron (XPS) spectroscopy measurements were carried out using a Thermo Scientific model K-Alpha spectrometer, equipped with an Al Kα X-ray source. All spectra were corrected using the C 1s peak with a binding energy of 284.6 eV. Transmission Electron Microscopy (TEM) was conducted on a JEOL JEM 2100 High Resolution Transmission Electron Microscope operated at 200 kV and equipped with an Oxford Instruments X-Max 80T Energy Dispersive Spectrometer (EDS) system. Carbon support film-coated copper TEM grids (200 mesh) were used to support the samples. HRTEM images were taken using a Gatan Model 794 Slow Scan CCD Camera.

Film morphologies were evaluated by Scanning Electron Microscopy (SEM) using a TESCAN Vega3 microscope. Diffuse Reflectance Spectra (DRS) were obtained using a UV 2600 spectrophotometer (Shimadzu) equipped with an integrating sphere. The electrochemical characterization was carried out on an Autolab PGSTAT204 (Metrohm) potentiostat/galvanostat equipped with an Electrochemical Impedance Spectroscopy (EIS) FRA32M module. The irradiation source was a 300 W Xe arc lamp (Oriel) equipped with an AM 1.5 G filter; the light intensity was measured using a power meter 1916-R (Newport) connected to an optical sensor 818-UV/DB.

A PTFE customized H-shaped photoelectrochemical cell was used for all (photo)electrochemical experiments. The catholyte chamber was filled with 0.1 M K$_2$SO$_4$ electrolyte and the anolyte chamber with glycerol 10% v/v in 0.1 M K$_2$SO$_4$ or bare flegmass with added 0.1 M K$_2$SO$_4$. Platinum was used as the counter electrode and Ag/AgCl as the reference electrode. A Nafion® proton selective membrane was placed between the anolyte and catholyte chambers. Backside illumination was provided through a 3.8 cm^2 quartz circular window placed at the front of the anolyte chamber.

The final composition of the anolyte was characterized by Chemical Oxygen Demand (COD), and the oxidation products were identified and quantified by High-Performance Liquid Chromatography (HPLC) and H^1 Nuclear Magnetic Resonance (NMR) analysis. HPLC analysis was performed on a Waters e2695 system equipped with a DAD-RID detector and using an Aminex HPX-87H column (300 × 7.8 mm, 5 μm) under isocratic conditions. The mobile phase was a mixture of MeCN : H$_2$O 35 : 65 (30 min) and H$_2$SO$_4$ (0.005 mol L^{-1}). A flow rate of 0.6 mL min^{-1} was employed, and the signals were detected at 254 nm. Quantification was made by calibration curves, obtained through the analysis of mixtures of chemical standards at known concentrations. H^1 NMR analyses were carried out on a Bruker spectrometer model Ascend 400 MHz, and dimethyl sulfoxide was used as an internal standard as described elsewhere.[5] All samples were filtered using PES 0.22 μm syringe filters. The gas products were identified and quantified using a Clarus 580 (PerkinElmer) GC-TCD equipped with a molecular sieve and a Porapak N packed column. Calibration curves, obtained by injecting known quantities of analytical grade H$_2$,

were used to quantify the green H_2 produced during the photoreforming assays.

Electron paramagnetic resonance (EPR) spectroscopy was conducted on solid photocatalyst powders to examine residual paramagnetic defects. EPR, combined with the spin trapping method, was utilized to explore the reaction mechanisms involved in the photocatalytic tests. For this purpose, the spin traps 5,5-dimethyl-1-pyrroline N-oxide (DMPO) and N-tert-butyl-α-phenylnitrone (PBN) were dissolved in distilled water and in a water/methanol mixture, respectively, with each solution containing 10% analytical glycerol. Different photocatalysts were then added to these solutions under magnetic stirring, and the samples were illuminated with a white LED lamp (16 mW cm^{-2}). At different time intervals, aliquots were taken, and EPR spectra were recorded. A similar procedure was performed using solutions without glycerol for comparison. Additionally, spin-trapping experiments were conducted using different $BiVO_4$ photoanodes paired with a Pt cathode under an applied bias and white light illumination. All EPR spectra were acquired using a Magnettech MiniScope MS 400 (Germany) at room temperature.

4 Conclusions

Niobium-doped $BiVO_4$ was synthesized *via* a facile hydrothermal method with varying niobium doping contents. Nb^{5+} occupied V^{5+} sites mainly at the surface, yielding oxygen vacancies, which are beneficial for the photoelectrochemical performance. The materials were then screen-printed into thin films and tested for the photoelectroreforming of real industrial biomass-derived wastes: crude glycerol and raw flegmass. The $BiVO_4$ sample doped with 5% Nb content demonstrated superior performance, converting 91.4% of glycerol with 88.9% selectivity toward formic acid formation after 5 hours of simulated sunlight illumination, achieving a low-carbon H_2 production rate of 4.2 µmol H_2 per cm^2 per h, 84% higher than that of unmodified monoclinic $BiVO_4$. 5% Nb : $BiVO_4$ photoanodes also exhibit better performance for flegmass photoelectroreforming, showing a sixfold increase in H_2 production and twice the COD removal efficiency compared to pristine $BiVO_4$. The improved performance of 5% Nb : $BiVO_4$ was attributed to increased charge density, decreased charge transfer resistance at the photoanode/electrolyte interface and surface defect states caused by Nb^{5+} doping. The present work brings a sustainable approach for green H_2 production using real industrial waste streams as a platform, an important step towards a cleaner society.

Conflicts of interest

There are no conflicts to declare.

Data availability

All data for this article have been included in the manuscript and the SI.

Supplementary information includes additional structural, morphological, and electrochemical characterizations (XPS, SEM/TEM-EDS, EIS), as well as product analyses (^{1}H NMR, HPLC) of crude glycerol and flegmass, supporting the findings of this study. See DOI: https://doi.org/10.1039/d5su00376h.

Acknowledgements

References

1 L. L. Nascimento, R. A. C. Souza, J. Z. Marinho, C. Wang and A. O. T. Patrocinio, *J. Clean. Prod.*, 2024, **449**, 141709.

2 Z. Tian, Y. Da, M. Wang, X. Dou, X. Cui, J. Chen, R. Jiang, S. Xi, B. Cui, Y. Luo, H. Yang, Y. Long, Y. Xiao and W. Chen, *Nat. Commun.*, 2023, **14**, 142.

3 D. A. Garcia-Osorio, T. P. Shalvey, L. Banerji, K. Saeed, G. Neri, L. J. Phillips, O. S. Hutter, C. Casadevall, D. Antón-García, E. Reisner, J. D. Major and A. J. Cowan, *Chem. Commun.*, 2023, **59**, 944–947.

4 J. Z. Marinho, L. L. Nascimento, A. L. R. Santos, A. M. Faria, A. E. H. Machado and A. O. T. Patrocinio, *Photochem. Photobiol. Sci.*, 2022, **21**, 1659–1675.

5 L. L. Nascimento, J. Z. Marinho, A. L. R. dos Santos, A. M. de Faria, R. A. C. Souza, C. Wang and A. O. T. Patrocinio, *Appl. Catal., A*, 2022, **646**, 118867.

6 D. Ouyang, F. Wang, D. Gao, W. Han, X. Hu, D. Qiao and X. Zhao, *iScience*, 2022, **25**, 105221.

7 X. Liang, T. Gao, Y. Cui, Q. Dong, X. Li, A. Labidi, E. Lichtfouse, F. Li, F. Yu and C. Wang, *Appl. Catal., B*, 2024, **357**, 124326.

8 Y. Miao, Z. Li, Y. Song, K. Fan, J. Guo, R. Li and M. Shao, *Appl. Catal., B*, 2023, **323**, 122147.

9 L. Luo, W. Chen, S.-M. Xu, J. Yang, M. Li, H. Zhou, M. Xu, M. Shao, X. Kong, Z. Li and H. Duan, *J. Appl. Chem. Sci.*, 2022, **144**, 7720–7730.

10 J. H. Kim, D. Hansora, P. Sharma, J.-W. Jang and J. S. Lee, *Chem. Soc. Rev.*, 2019, **48**, 1908–1971.

11 D. Chen, Z. Xie, Y. Tong and Y. Huang, *Energy Fuels*, 2022, **36**, 9932–9949.

12 G. Ke, F. Duan, B. Liu, X. Liu, J. Wen, B. Jia, X. Liu, H. He and Y. Zhou, *J. Alloys Compd.*, 2023, **934**, 167883.

13 S. S. Kalanur and H. Seo, *J. Catal.*, 2022, **410**, 144–155.

14 X. Wu, N. Luo, S. Xie, H. Zhang, Q. Zhang, F. Wang and Y. Wang, *Chem. Soc. Rev.*, 2020, **49**, 6198–6223.

15 W. essie, X. Luo, F. He, Y. Liao, G. J. Duns and Z. Qin, *Biocatal. Agric. Biotechnol.*, 2023, **51**, 102777.

16 M. Zhang, H. Xu, L. Wu, Y. Tan, D. Kong and M. Yimiti, *New J. Chem.*, 2022, **46**, 8644–8652.

17 D. Guo, M. Hu, Z. Chen, B. Cui, Q. Zhang, Y. Liu, S. Luo, R. Ruan and Y. Liu, *Bioresour. Technol.*, 2020, **315**, 123831.

18 D. K. Bora, M. Nadjafi, A. Armutlulu, D. Hosseini, P. Castro-Fernández and R. Toth, *Energy Adv.*, 2022, **1**, 715–728.

19 D. Liu, J.-C. Liu, W. Cai, J. Ma, H. B. Yang, H. Xiao, J. Li, Y. Xiong, Y. Huang and B. Liu, *Nat. Commun.*, 2019, **10**, 1779.

20 A. C. M. Loy, W. L. Ng, S. P. Samudrala and S. Bhattacharya, *Sustainable Energy Fuels*, 2023, **7**, 2653–2669.

21 OECD and Food and A. O. o. t. U. Nations, *OECD-FAO Agricultural Outlook 2016-2025*, 2016.

22 P. Ribao, M. A. Esteves, V. R. Fernandes, M. J. Rivero, C. M. Rangel and I. Ortiz, *Int. J. Hydrogen Energy*, 2019, **44**, 28494–28506.

23 M. Zielińska, K. Bułkowska and W. Mikucka, *Energies*, 2021, **14**, 7235.

24 National Company of Supplying (CONAB), *Cenários de Oferta de Etanol e Demanda de Ciclo Otto 2021-2030*, Brazília, 2024.

25 W. C. Kee, Y. S. Wong, S. A. Ong, N. A. Lutpi, S. T. Sam, A. Chai and K. M. Eng, *Int. J. Environ. Res.*, 2022, **16**, 3.

26 T. S. Dabodiya, P. Selvarasu and A. V. Murugan, *Inorg. Chem.*, 2019, **58**, 5096–5110.

27 O. F. Lopes, K. T. G. Carvalho, A. E. Nogueira, W. Avansi and C. Ribeiro, *Appl. Catal., B*, 2016, **188**, 87–97.

28 S. Obregón, A. Caballero and G. Colón, *Appl. Catal., B*, 2012, **117–118**, 59–66.

29 Y. Zhang, S. Liu, Q. Zhang, T. Ning, X. Wang and A. Lu, *J. Alloys Compd.*, 2022, **902**, 163760.

30 X. Yang, S. Liang, J. Miao, Y. Yang and S. Zhang, *Chemphyschem*, 2025, **26**, e202400692.

31 T. S. Dabodiya, T. George, F. A. Mathew and A. V. Murugan, *ACS Appl. Energy Mater.*, 2024, **7**, 2309–2328.

32 D. Xiao, G. Cheng, H. She, X. Chen, J. Huang, L. Wang and Q. Wang, *J. Phys. Chem. C*, 2024, **128**, 15266–15276.

33 T. Wang, C. Feng, J. Liu, D. Wang, H. Hu, J. Hu, Z. Chen and G. Xue, *Chem. Eng. J.*, 2021, **414**, 128827.

34 F. A. Qaraah, S. A. Mahyoub, A. Hezam, W. Zhang, G. Xiu, J. Munyaneza and C. Wu, *RSC Adv.*, 2020, **10**, 32309–32322.

35 M. Zubair, G. Li, B. Wang, L. Wang and H. Yu, *ACS Appl. Energy Mater.*, 2019, **2**, 503–512.

36 K. Wannakan, K. Khansamrit, T. Senasu and S. Nanan, *ACS Omega*, 2023, **8**, 4835–4852.

37 K. Pingmuang, A. Nattestad, W. Kangwansupamonkon, G. G. Wallace, S. Phanichphant and J. Chen, *Appl. Mater. Today*, 2015, **1**, 67–73.

38 S.-H. Chen, Y.-S. Jiang and H.-y. Lin, *ACS Omega*, 2020, **5**, 8927–8933.

39 H. S. Park, K. E. Kweon, H. Ye, E. Paek, G. S. Hwang and A. J. Bard, *J. Phys. Chem. C*, 2011, **115**, 17870–17879.

40 K. T. Drisya, M. Solís-López, J. J. Ríos-Ramírez, J. C. Durán-Álvarez, A. Rousseau, S. Velumani, R. Asomoza, A. Kassiba, A. Jantrania and H. Castaneda, *Sci. Rep.*, 2020, **10**, 13507.

41 G. R. Buettner, *Free Radical Biol. Med.*, 1987, **3**, 259–303.

42 D. R. C. M. DuBose, U. M. Oehler and E. G. Janzen, *Free Radical Biol. Med.*, 1988, **5**, 55–56.

43 H. Tateno, S.-Y. Chen, Y. Miseki, T. Nakajima, T. Mochizuki and K. Sayama, *ACS Sustain. Chem. Eng.*, 2022, **10**, 7586–7594.

44 D. W. Skaf, N. G. Natrin, K. C. Brodwater and C. R. Bongo, *Catal. Lett.*, 2012, **142**, 1175–1179.

45 J. G. Villachica-Llamosas, J. Sowik, A. Ruiz-Aguirre, G. Colón, J. Peral and S. Malato, *J. Environ. Chem. Eng.*, 2023, **11**, 111216.

46 Y.-H. Wu, D. A. Kuznetsov, N. C. Pflug, A. Fedorov and C. R. Müller, *J. Mater. Chem. A*, 2021, **9**, 6252–6260.

47 N. Hedayat, Y. Du and H. Ilkhani, *Renew. Sustain. Energy Rev.*, 2017, **77**, 1221–1239.

48 C. Günnemann, M. Curti, J. G. Eckert, J. Schneider and D. W. Bahnemann, *ChemCatChem*, 2019, **11**, 6439–6450.